INTERNATIONAL JOURNAL FOR NUMERICAL METHODS IN FLUIDS, VOL. 21, 237–251 (1995)

NUMERICAL STUDY OF A PISTON-DRIVEN UNSTEADY FLOW IN A PIPE WITH SUDDEN EXPANSION

H. STRÖLL

Wehrtechnische Dienststelle für Fernmeldewesen und Elektronik, D-91171 Greding, Germany

F. DURST

Lehrstuhl für Strömungsmechanik der Universität Erlangen-Nürnbuerg, Cauerstraße 4, D-91058 Erlangen, Germany

M. PERIĆ

Institut für Schiffbau der Universität Hamburg, Lämmersieth 90, D-22305 Hamburg, Germany

AND

G. SCHEUERER

Advanced Scientific Computing G.m.b.H., Münchner Straße 3, D-83607 Holzkirchen, Germany

SUMMARY

This paper presents results of the numerical study of a piston-driven unsteady flow in a pipe with sudden expansion. The piston closes the larger-diameter pipe and moves between two limiting positions with strong acceleration or deceleration at the beginning and end of each stroke and constant velocity in between. The piston velocity in the exhaust stroke is about four times higher than in the intake stroke. Periodic piston movement in this fashion creates a complex unsteady flow between the piston head and the plane of sudden expansion. The numerical method is implicit and of finite volume type, using a moving grid and a collocated arrangement of variables. Second-order spatial discretization, fine grids and a multigrid solution method were used to ensure high accuracy and good efficiency. Spatial and temporal discretization errors were of the order of 1% and 0·1% respectively. The features of the flow are discussed and the velocity profiles are compared with experimental data, showing good qualitative and quantitative agreement.

KEY WORDS: finite volume; multigrid; unsteady flow

INTRODUCTION

Accurate numerical solutions of practical flow problems require the use of fine numerical grids. Unsteady separated flows are especially demanding in this respect. In such flows the time-dependent movement of vortices makes practices such as grid contraction and local refinement not very useful: accurate solutions can only be achieved by using globally fine grids. With standard iterative methods this approach soon beomes prohibitively expensive, as the computing times vary proportionally with the square of the number of grid nodes.

During the last 10 years the multigrid technique has evolved as a powerful tool for accelerating the convergence of iterative methods. For linear problems, multigrid methods are asymptotically optimal, i.e. the computing times are directly proportional to the number of grid points. Brandt and Dinar,[1] Vanka,[2] Wittum,[3] Barcus *et al.*[4] and Hortmann *et al.*,[5] among others, have shown that these features are also valid for the solution of non-linear problems, namely the incompressible Navier–Stokes

CCC 0271–2091/95/030237–15

Received June 1994
Revised January 1995

equations. For steady laminar flow problems, computing time reductions of up to two orders of magnitudes were reported for grids with 10^4–10^5 grid points.

Unsteady flows—especially those exhibiting periodicity—often require very fine numerical grids for an adequate spatial resolution of vortices, but allow for larger time steps or lower-order temporal discretization. For such cases, explicit schemes are inefficient, since the limiting time step size is proportional to the square of the mesh spacing. Such methods thus become extremely restrictive when very fine resolution is required. Implicit schemes, on the other hand, are less prohibitive regarding the time step size, but require outer iterations within each time step to solve a non-linear system of equations. The effectiveness of an implicit method is then crucially dependent on the efficiency of the iterative solution scheme.

In the present paper the efficiency of a fully implicit solution method coupled with a multigrid outer iteration scheme is demonstrated by solving unsteady flow problems where spatial resolution is the limiting factor for accuracy. An extension of the previously reported solution method for moving grids[6,7] is used to predict unsteady piston-driven flows in a pipe with sudden expansion. The solution method is of finite volume type and uses a collocated variable arrangement. The convection, diffusion and source terms are discretized using second-order central difference approximations. Time discretization is first-order fully implicit (Euler scheme). Pressure–velocity coupling is achieved via the SIMPLE algorithm.[8] A multigrid method based on a full approximation scheme (FAS) is implemented to accelerate the outer iterations within each time step,[5] while the linear equations are relaxed on all grid levels by the ILU solver of Stone,[9] which is based on incomplete lower–upper decomposition. Estimation of spatial and temporal discretization errors is used as guidance in selecting grid and time step sizes.

In the next section the solution method is briefly outlined; more details can be found in References 5–7. This is followed by a description of the flow problem under investigation, a demonstration of the efficiency of the solution method and an error analysis. Finally, results of calculations are presented and compared with experimental data.

NUMERICAL METHOD

The flow of an incompressible fluid in a domain with moving boundaries is governed by the conservation equations for space, mass and momentum, which for an incompressible Newtonian fluid with constant properties read[7]

$$\frac{\mathrm{d}}{\mathrm{d}t}\int_\Omega \mathrm{d}\Omega - \int_S \mathbf{v}_\mathrm{b}\cdot\mathbf{n}\,\mathrm{d}S = 0, \tag{1}$$

$$\frac{\mathrm{d}}{\mathrm{d}t}\int_\Omega \rho\,\mathrm{d}\Omega + \int_S \rho(\mathbf{v}-\mathbf{v}_\mathrm{b})\cdot\mathbf{n}\,\mathrm{d}S = 0, \tag{2}$$

$$\frac{\mathrm{d}}{\mathrm{d}t}\int_\Omega \rho u_i\,\mathrm{d}\Omega + \int_S \rho u_i(\mathbf{v}-\mathbf{v}_\mathrm{b})\cdot\mathbf{n}\,\mathrm{d}S = \int_S \mu\nabla u_i\cdot\mathbf{n}\,\mathrm{d}S + \int_\Omega b_i\,\mathrm{d}\Omega, \tag{3}$$

where ρ represents the fluid density, μ is the dynamic viscosity, $\mathbf{v}$ is the fluid velocity vector with Carteisn or cylindrial components u_i, $\mathbf{v}_\mathrm{b}$ is the velocity of the control volume boundary, b_i is the body force in the ith co-ordinate direction, Ω is the volume and S is the surface of the control volume. When using cylindrical co-ordinates for two-dimensional studies of pipe flows, the body force contains—in addition to the pressure gradient in the corresponding co-ordinate direction—the term $\mu u_r/r^2$ in the equation for the radial velocity component.

The above equations are discretized on rectangular control volumes (CVs); see Figure 1. In the case to be studied, the grid moves only in the x-direction (in one part of the solution domain). The position

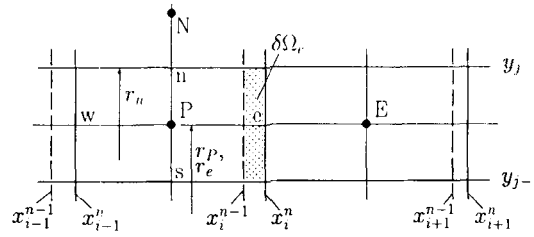

Figure 1. Typical control volume and notation used

of the grid lines is specified as a function of time, so that at any time t_n the co-ordinates x_i and y_j are known for both t_n and t_{n-1}. The space conservation law (1) then reduces to[7] (see Figure 1)

$$\int_{S_e} \mathbf{v}_b \cdot \mathbf{n}\, dS \approx \frac{\delta\Omega_e}{\Delta t} = \frac{(x_i^n - x_i^{n-1})(y_j - y_{j-1})r_e}{\Delta t}. \tag{4}$$

Here, as well as in other rate-of-change terms, first-order fully implicit time discretization is employed. The same expressions are valid for both Cartesian and cylindrical geometries; in the former case $r=1$ and in the latter case $r=y$. The mass fluxes through the east and north CV faces are calculated as

$$\dot{m}_e = \int_{S_e} \rho(\mathbf{v} - \mathbf{v}_b) \cdot \mathbf{n}\, dS \approx \rho r_e \left[u_x(y_j - y_{j-1}) - \frac{(x_i^n - x_i^{n-1})(y_j - y_{j-1})}{\Delta t} \right]_e, \tag{5}$$

$$\dot{m}_n = \int_{S_n} \rho(\mathbf{v} - \mathbf{v}_b) \cdot \mathbf{n}\, dS = [\rho r u_y (x_i - x_{i-1})]_n. \tag{6}$$

Note that the grid velocity vector has only the x-component in equation (6), otherwise an additional term similar to that in equation (5) would result for the north side too. Also note that in the part of the solution domain with fixed grid, $x_i^{n-1} = x_i^n$, so that the contribution to the mass flux through the east CV face from the moving grid disappears and the usual expression for fixed grids results; cf. equation (6). In the above and all other similar expressions, surface integrals are approximated by assuming that the variable values at the centre of the CV face are the mean values over the whole face. This is second-order approximation provided that the values at the CV face centre (which are not known) are expressed through the nodal values by means of an approximation of at least second order. In this work, central differences (linear interpolation) are used throughout, thus resulting in overall spatial discretization of second order. Convection fluxes of the momentum components are evaluated as e.g.

$$F_{i,e}^c = \int_{S_e} \rho u_i (\mathbf{v} - \mathbf{v}_b) \cdot \mathbf{n}\, dS \approx \dot{m}_e u_{i,e}. \tag{7}$$

This is the simplest linearization of the non-linear convection terms in the Navier–Stokes equations (Picard iteration scheme). The cell face values are obtained by linear interpolation of the immediate neighbour values. This approximation is implemented using the 'deferred correction' approach.[10]

Diffusion fluxes are approximated as

$$F_{i,e}^d = \int_{S_e} \mu \nabla u_i \cdot \mathbf{n}\, dS \approx \frac{\mu(y_j - y_{j-1})r_e}{\frac{1}{2}(x_{i+1}^n - x_{i-1}^n)} (u_{i,E} - u_{i,P}). \tag{8}$$

Volume integrals are approximated by assuming that the value of the integrand at the CV centre represents the mean value over the whole CV; these values are then simply multiplied by the cell volume $\Delta\Omega$. The rate-of-change term is approximated as

$$\frac{d}{dt}\int_\Omega \rho u_i\, d\Omega \approx \frac{(\rho u_i \Delta\Omega)^n - (\rho u_i \Delta\Omega)^{n-1}}{\Delta t}. \tag{9}$$

When all terms are assembled so that implicit parts are on the left-hand side and explicit parts on the right-hand side of the balance equation for each CV, an algebraic equation of the form

$$A_{\mathrm{P}} u_{i,\mathrm{P}} + \sum_{nb} A_{nb} u_{i,nb} = Q_i \tag{10}$$

results, where the index '*nb*' runs over the four intermediate neighbours E, W, N and S; see Figure 1. For the solution domain as a whole and a structured grid a matrix equation with diagonal structure results, which is solved for given coefficients by the iterative solver of Stone.[9]

Adopting the SIMPLE algorithm for pressure–velocity coupling, the continuity equation is transformed into a pressure correction equation,[7] which has the same discretized form as equation (10). The source term of this equation is the mass imbalance after solving the momentum equations plus the rate of change due to volume change:

$$Q_{\mathrm{m}} = \frac{(\rho \Delta \Omega)^n - (\rho \Delta \Omega)^{n-1}}{\Delta t} + \dot{m}_{\mathrm{e}} + \dot{m}_{\mathrm{w}} + \dot{m}_{\mathrm{n}} + \dot{m}_{\mathrm{s}}. \tag{11}$$

At boundary cell faces the fluxes have to be either specified or calculated using specified boundary values of the dependent variable and one-sided differences for gradient approximations. At walls the convection fluxes in the momentum equations are equal to zero. The diffusion flux of the tangential velocity component is calculated at walls using the prescribed wall velocity (no-slip condition) and a linear profile assumption. For the normal velocity component the diffusion flux at walls is set to zero, since the normal stress is zero there. In axisymmetric geometries all fluxes are equal to zero at the symmetry axis, since the area of the cell face is equal to zero. In plane geometries the mass fluxes and convection fluxes in the momentum equations are equal to zero at symmetry planes. The diffusion flux of the tangential velocity component is also equal to zero there, since the shear stress vanishes in a symmetry plane. The diffusion flux of the normal velocity component is calculated at symmetry planes using a zero boundary value of the normal velocity and a linear profile assumption. At the inlet the mass fluxes and both velocity components are prescribed. The diffusion fluxes are calculated using specified velocity values and a linear profile assumption. At the outlet the velocities are extrapolated (usually using a zero-gradient assumption if the outlet is far downstream). The diffusion fluxes are usually neglected at the outlet.

For the pressure correction equation the specified mass flux through the boundary cell face implies zero gradient of the pressure correction in the normal direction. Even at the outlet the mass fluxes (calculated using extrapolated velocities and corrected to satisfy global mass conservation) are frozen within one SIMPLE iteration, so that the pressure correction equation has Neumann conditions at all boundaries. The sum of source terms then has to be equal to zero (which is ensured by the above-mentioned correction at the outlet) and the solution is unique only in terms of gradients, which is all that is needed.

Sequential solution of the equations for u_i and pressure correction is repeated until the sum of the absolute residuals (calculated with the new coefficients and prevailing solution) over all CVs for each variable has fallen by at least three orders of magnitude. One inner iteration in the solver is performed for the velocity components per outer iteration (coefficient update) and up to 10 inner iterations for the pressure correction equation; the latter requires more iterations since it has Neumann boundary conditions along all boundaries and hence converges more slowly.[7]

In order to reduce the number of outer iterations per time step, the FAS multigrid algorithm is employed. The solution for a new time step is started on the finest grid using variable values from the previous time step as the initial guess. After three to five outer iterations the solution process is transferred to the next coarser grid, where equations for the full approximations of the fine grid solution are solved.[5] This sequence is repeated until the coarest grid is reached; the process is then

repeated in reversed order (V-cycle). The coarse grids produce a correction for the fine grid solution if the residuals on the finest grid are non-zero. Full details of the algorithm are available in Reference 11.

In the next section the test case and the boundary conditions are presented, together with some details of the calculation.

TEST CASE AND ACCURACY ANALYSIS

The geometry and dimensions of the solution domain for the test case studied here are shown in Figure 2. The flow is induced by the piston movement between the minimum and maximum clearances $x_{p,min}$ and $x_{p,max}$ respectively. In the intake stroke the piston accelerates strongly and within 0·05 s reaches a velocity of 6·22 mm s^{-1}, which remains constant until 0·05 s before top dead centre (TDC). In the exhaust stroke the piston accelerates even more strongly and after 0·18 s reaches its maximum velocity of $-26{\cdot}5$ mm s^{-1}, which remains constant until 0·18 s before bottom dead centre (BDC), where deceleration starts. The whole cycle lasts 3·8 s. The piston velocity U_p (mm s^{-1}) as a function of time t (s) can be expressed as follows:

$$U_p = \begin{cases} 124{\cdot}4t & \text{for } 0 \leqslant t \leqslant 0{\cdot}05, \\ 6{\cdot}22 & \text{for } 0{\cdot}05 \leqslant t \leqslant t_{TDC} - 0{\cdot}05, \\ 6{\cdot}22 - 124{\cdot}4(t_{TDC} - t) & \text{for } t_{TDC} - 0{\cdot}05 \leqslant t \leqslant t_{TDC}, \\ -14.7222(t - t_{TDC}) & \text{for } t_{TDC} \leqslant t \leqslant t_{TDC} + 0{\cdot}18, \\ -26{\cdot}5 & \text{for } t_{TDC} + 0{\cdot}18 \leqslant t \leqslant t_{BDC} - 0{\cdot}18, \\ -26{\cdot}5 + 14{\cdot}7222(t_{BDC} - t) & \text{for } t_{BDC} - 0{\cdot}18 \leqslant t \leqslant t_{BDC}. \end{cases}$$

These relations approximate closely the piston velocity recorded in the experiments of Durst *et al.*[12] The Reynolds numbers in the intake and exhaust strokes (based on the larger pipe diameter) are 72 and 306 respectively, yielding laminar flow conditions. Experiments were repeated periodically. The calculations were performed over three full cycles.

In the acceleration/deceleration phase of the intake stroke the time step size varies in the form of a geometrical series from 0·0001 to 0·005 s. During the phase of constant velocity the time step size varies between 0·005 and 0·02 s. In the acceleration/deceleration phase of the exhaust stroke the time step size varies between 0·0001 and 0·002 s. The time step is kept constant at $\Delta t = 0{\cdot}002$ s during the phase of constant exhaust velocity. These time step sizes ensure that the Courant number always stays below unity on the finest grid. The analysis of the time discretization errors showed that these time steps were adequate for a sufficiently accurate resolution of the unsteady fluid motion.

The velocity at the inlet to the small pipe is adjusted in each time step to satisfy global mass conservation: the volumetric flow through the inlet cross-section must equal the volume change in the large pipe due to piston displacement, since the fluid is incompressible. In the first cycle a block profile is specified at the inlet. During the exhaust stroke the velocity is extrapolated to the outlet boundary and corrected to obey global mass conservation. Since the flow in the small-diameter pipe is fully developed up to about one diameter before the sudden expansion, extrapolation is used in the intake

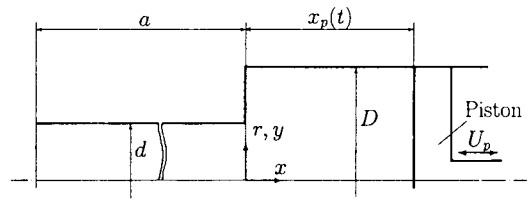

Figure 2. Geometry of solution domain: $D = 45$ mm, $d = 19$ mm, $a = 100$ mm

and exhaust strokes in all subsequent cycles. The flow is found to repeat from the second cycle onwards.

A sequence of four systematically refined non-uniform grids with 32 × 10, 64 × 20, 128 × 40 and 256 × 80 CVs is used. One coarser grid CV is made of four finer grid CVs. Calculations were performed for the first intake stroke using three and four grid levels and the same time step sizes. By comparing the solutions from the two finest grids at given times, one can estimate spatial discretization errors (we assume that the temporal discretization error is of the same order on both grids, since the time step is the same). For a second-order scheme and sufficiently fine grids the discretization error on the finer grid is approximately equal to one-third of the difference between the two solutions. In this way the spatial discretization errors were estimated for several piston positions. Figure 3 shows contours of constant error for normalized piston displacements s_p^+ of 0·13, 0·34 and 0·89 ($s_p = 0$ at BDC and $s_p = 1$ at TDC; superscripts '+' and ' − ' denote intake and exhaust strokes respectively). Regions in which the error is higher than 3% of the average inlet velocity are shaded. These figures clearly indicate that the errors are generated at the sudden expansion in the early stage of the stroke and are then convected downstream. The peaks in the discretization errors correspond to regions of high change in velocity gradients, as will become apparent from velocity profiles and streamline plots to be shown later.

Time discretization errors can be estimated in a similar way by performing calculations on the same grid but using systematically refined time steps. Here the calculations were done on the finest grid up to a piston displacement $s_p^+ = 0{\cdot}1$ using constant time steps of 0·002, 0·001, 0·0005 and 0·00025 s. From the difference in the solutions at the same piston position obtained with consecutive time steps the expected behaviour of a first-order time discretization scheme was confirmed: the error was reducing by a factor of two when the time step was halved. The error with the smaller time step is thus

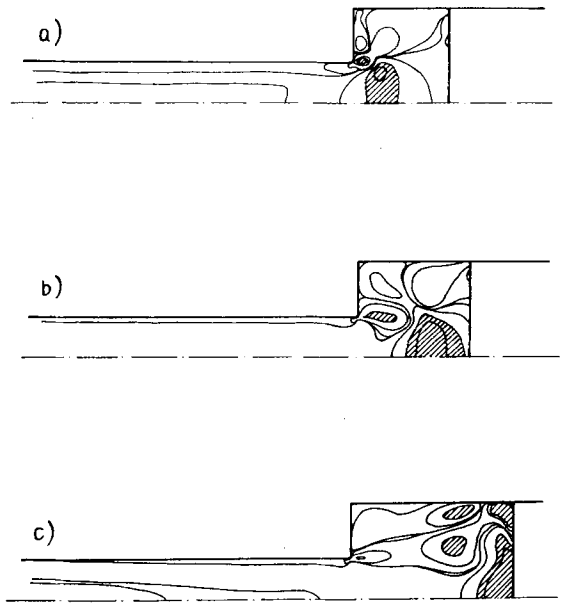

Figure 3. Distribution of spatial discretization error for different piston locations during intake stroke: (a) $s_p^+ = 0{\cdot}11$; (b) $s_p^+ = 0{\cdot}30$; (c) $s_p^+ = 0{\cdot}92$ (shaded regions are where error is larger than 3% of mean inlet velocity)

approximately equal to the difference between the two solutions. The analysis showed that the temporal discretization errors were of the order of 0·1% for the time step size chosen for the calculation of the whole cycle, which is an order of magnitude lower than the spatial discretization errors. This justifies the choice of a first-order implicit scheme for temporal discretization.

For the chosen finest grid and time steps, calculations were performed in parallel with the single-grid (SG) and multigrid (MG) algorithms up to $s_p^+ = 0{\cdot}1$. For the first 50 time steps, calculations were also performed on the next finer grid with 512 × 160 CVs in order to test the efficiency of the multigrid algorithm. Table I gives the computing times on a Cyber 995E computer for the first and 22nd time steps for both methods. The computing time on the fifth grid for the SG version was estimated by performing 200 outer iterations and then extrapolating, assuming a constant convergence rate. For all time steps the MG method required one-twentieth to one-fiftieth of the time required by the SG method.

In order to illustrate why the MG method is more efficient, the convergence error (the difference between the converged solution for a given time step and the intermediate solution after a certain number of outer iterations) was evaluated and plotted in Figures 4 and 5. Figure 4 shows convergence errors for the axial velocity component after 10, 100, 400 and 800 outer iterations on the finest grid when the SG algorithm is used. The spatial distribution of the error shows one long-wave component and some short-wave oscillations at the corner of the sudden expansion. Both the long-wave and short-wave components are visible even after 400 outer iterations; only after 800 iterations is the error reduced everywhere below the specified level. Figure 5 shows the same information for the MG method (note that the scale is not the same in each plot). After the third outer iteration on the finest grid, one V-cycle through all grids is performed. The correction for the fine grid solution calculated on coarser grids eliminates the long-wave error component almost completely, as can be seen from the error plot after the fourth iteration on the finest grid. Only some short-wave noise, mostly resulting from interpolation errors, remains. After one more V-cycle is performed, only a small error in the plane of sudden expansion remains (see the error after the eighth iteration in Figure 5). Finally, after the third V-cycle (after the 12th iteration on the finest grid) the iteration error is as small as in the single-grid method after 800 iterations. This is the well-known feature of multigrid iterative methods for linear problems, which apparently applies also to outer iterations for coupled equation systems.[1–4]

With the MG method, on average about 10–15 outer iterations were performed per time step. Within each outer iteration, only one inner iteration with Stone's solver was performed for the velocity components and five to 10 for the pressure correction. At the end of each time step the mass conservation equation and the non-linear momentum equations were satisfied to within four most significant digits.

Table I. Computing times for single-grid and multigrid solution methods on a Cyber 995E computer

Time step	Solution method	Computing time for various grids (s)				
		32 × 10	64 × 20	128 × 40	256 × 80	512 × 160
1	SG	1·3	7·3	268·0	3413·9	2000000*
	MG	1·3	3·8	14·8	66·8	305·5
22	SG	0·8	1·8	108·2	1351·3	60000*
	MG	0·8	1·3	9·1	49·8	232·4

* Estimated values.

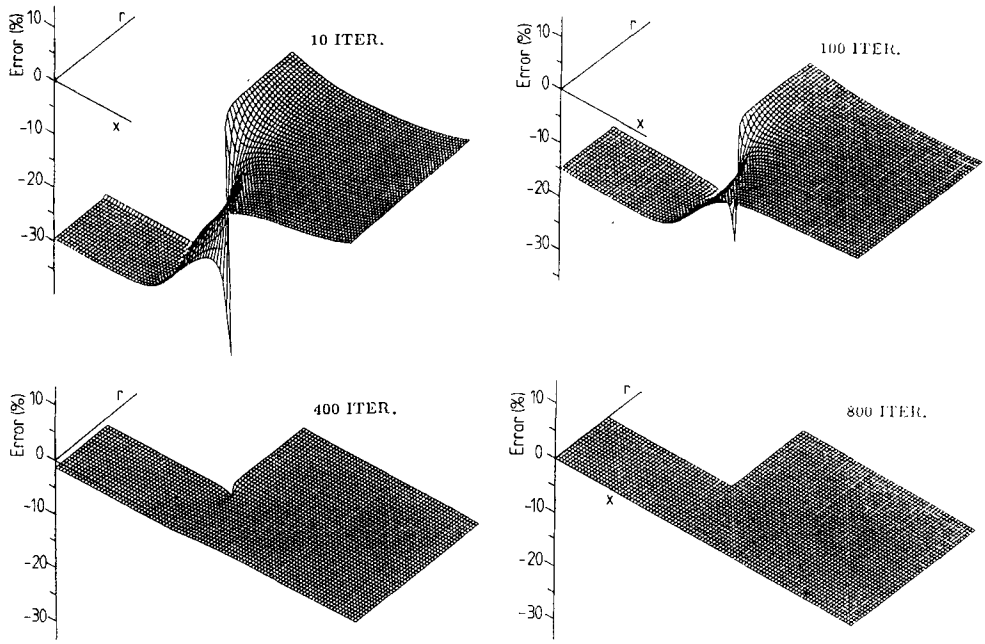

Figure 4. Convergence error for axial velocity and SG algorithm after various numbers of outer iterations during first time step (percentage of mean inlet velocity)

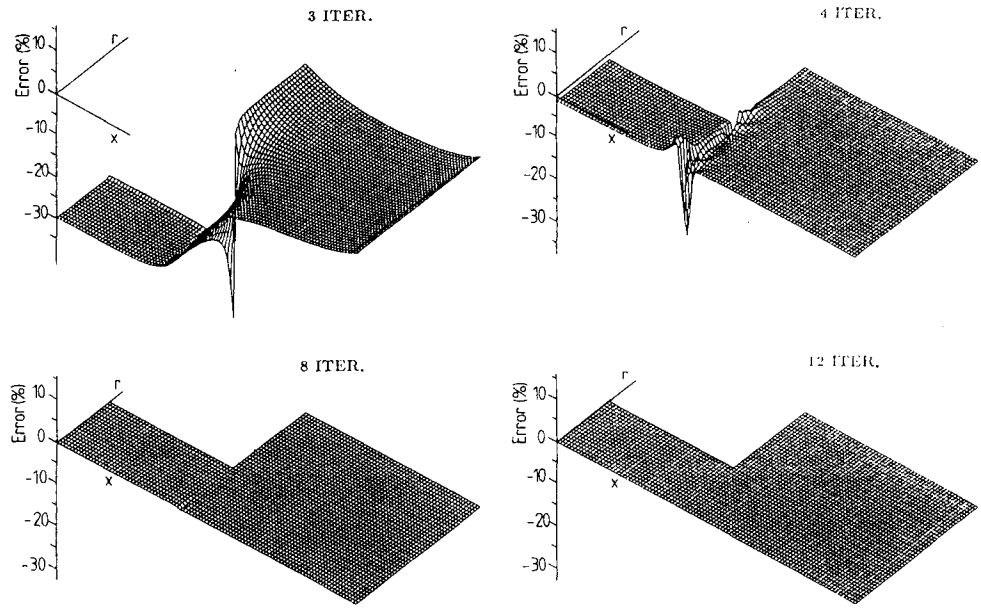

Figure 5. Convergence error for axial velocity and MG algorithm after various numbers of outer iterations within one time step (percentage of mean inlet velocity)

RESULTS AND COMPARISON WITH EXPERIMENT

Having ensured satisfactory numerical accuracy of the results, calculations were performed for three cycles of intake and exhaust strokes in a configuration with minimum and maximum piston displacements of 21 and 41 mm respectively. Figure 6 shows streamlines at some piston positions within the second cycle. The third cycle is identical with the second one, while the first one differs in the intake and first half of the exhaust stroke. At $s_p^+ = 0{\cdot}12$ the vortex generated during the exhaust stroke has almost disappeared and a new vortex is generated behind the sudden expansion. This vortex grows in strength and size; its centre travels with approximately doubled piston velocity towards the piston heat. At TDC it occupies the whole cylinder. A special feature of the flow is an oblique wave in the streamline pattern behind the primary vortex, which can be seen in the plots for $s_p^+ = 0{\cdot}12$ and $0{\cdot}30$ and which did not exist in the first cycle. This might be the first sign of instability, which was observed by the experimenters for intake velocities higher than 7 mm s^{-1} and which caused cycle-to-cycle variations and three-dimensionality of the flow.[11] The source of this phenomenon lies in the sudden suction of the central vortex which occupies the central part of the cylinder at the end of the exhaust stroke. The flow in the small pipe quickly becomes fully developed again when the piston achieves its constant speed during the intake stroke, as indicated by the parallel streamlines in Figures 6(a)–6(c). The areas of largest discretization errors coincide with the position of the waves; see Figure 3. It is also interesting to note that the big vortex at the end of the intake stroke completely disappears at $s_p^- = 0{\cdot}34$ in the exhaust stroke. Thereafter two new vortices are created; see Figure 6(g). The reason for this is that the linear motion of the piston head is displacing more volume at a larger radius and the fluid from the outer region has to be accelerated to enter the small-diameter pipe. When the piston comes close to the plane of sudden expansion, the streamline curvature and acceleration creates a radial pressure gradient which causes fluid in the centreline region to recirculate. At this stage a recirculation is also

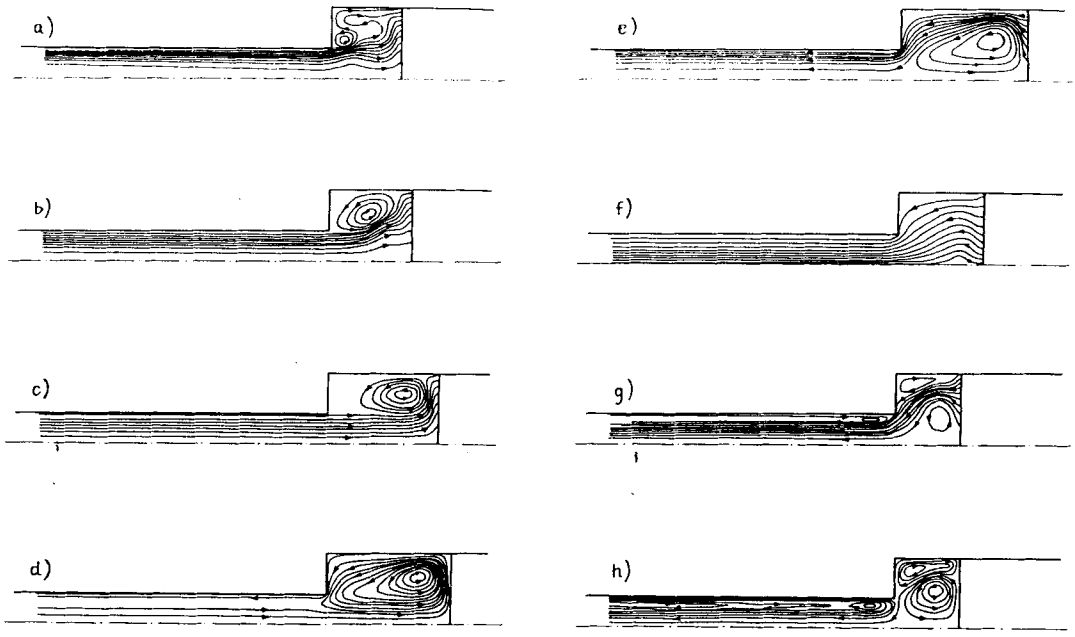

Figure 6. Streamlines during intake and exhaust strokes in second cycle at different piston positions (initial piston clearance 21 mm, stroke 20 mm): (a) $s_p^+ = 0{\cdot}12$; (b) $s_p^+ = 0{\cdot}30$; (c) $s_p^+ = 0{\cdot}78$; (d) $s_p^+ = 1{\cdot}00$; (e) $s_p^- = 0{\cdot}99$; (f) $s_p^- = 0{\cdot}34$; (g) $s_p^- = 0{\cdot}05$; (h) $s_p^- = 0{\cdot}00$.

created in the small-diameter pipe owing to the contraction of the jet-like flow in the sudden constriction area; see Figure 6(g).

This flow pattern is not in all details representative of all piston-driven flows, although the main features remain the same. In the case of a larger clearance at BDC (minimum piston displacement 42 mm, maximum 60 mm) the central vortex does not disappear but remains attached to the symmetry line during the whole exhaust stroke; see Figures 7(f)–7(i). During the intake stroke this vortex is lifted from the symmetry line by the sucked-in fluid and persists until $s_p^+ \approx 0{\cdot}5$; see Figure 7(c). The wave in the streamline pattern is present in this case too, as can be seen from Figures 7(a)–7(c). At $s_p^+ = 0{\cdot}01$ one can see the leftovers of the small-pipe vortex from the end of the exhaust stroke being washed away, as well as the build-up of waves shortly before the sudden expansion.

The numerical solutions were found to describe these complex flows qualitatively and quantitatively correctly. In Figure 8 the computed and measured axial and radial velocities are compared at various radial cross-sections for $s_p^+ = 0{\cdot}69235$ in the intake stroke. At this stage a large vortex is present in the outer region of the cylinder; see Figures 6(b) and 6(c). All features of the velocity profiles, including the inflection points, are correctly predicted. Only the maximum negative axial velocity is appreciably underpredicted between $x = 0{\cdot}02$ and $0{\cdot}03$ m. The small area of the peak velocity lies in the region where the discretization error was predicted to be above 1%; locally larger errors are possible, so that some improvement in peak resolution could be expected after further grid refinement. Another reason for disagreement might lie in experimental uncertainty or flow asymmetry, as suggested by disturbances in the measured data at the symmetry line in the profiles at $x = 0{\cdot}026$ and $0{\cdot}029$ m; see Figure 8.

In Figure 9 the computed and measured axial and radial velocities are compared at various radial cross-sections for $s_p^- = 0{\cdot}2938$ in the exhaust stroke. At this stage the central vortex at the symmetry

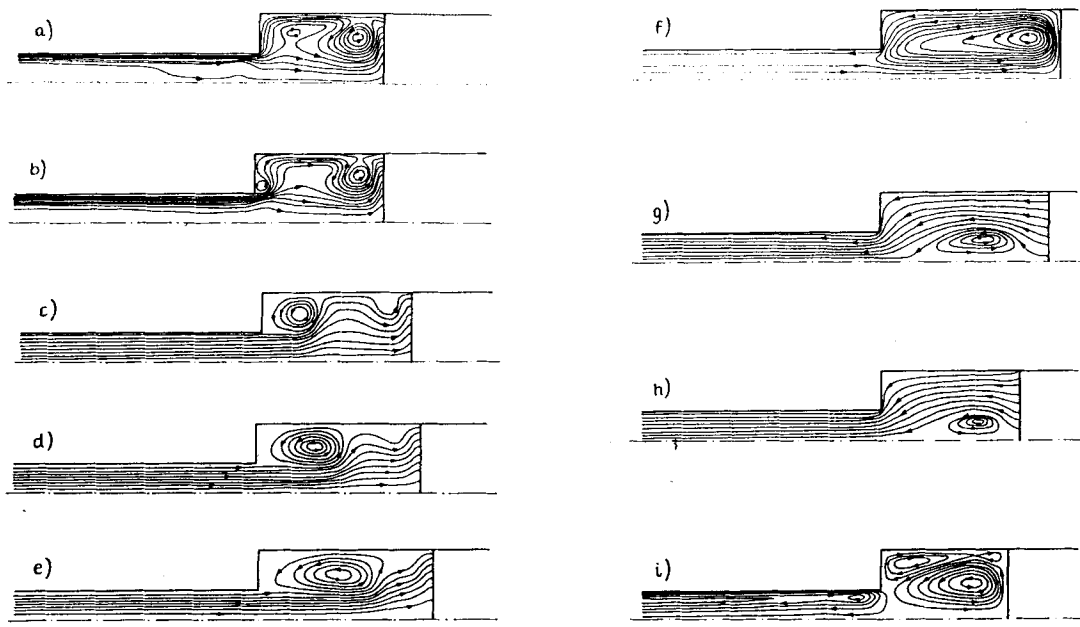

Figure 7. Streamlines during intake and exhaust strokes in second cycle at different piston positions (initial piston clearance 42 mm, stroke 18 mm): (a) $s_p^+ = 0{\cdot}01$; (b) $s_p^+ = 0{\cdot}10$; (c) $s_p^+ = 0{\cdot}49$; (d) $s_p^+ = 0{\cdot}74$; (e) $s_p^+ = 0{\cdot}94$; (f) $s_p^+ = 1{\cdot}00$; (g) $s_p^- = 0{\cdot}81$; (h) $s_p^- = 0{\cdot}22$; (i) $s_p^- = 0{\cdot}00$.

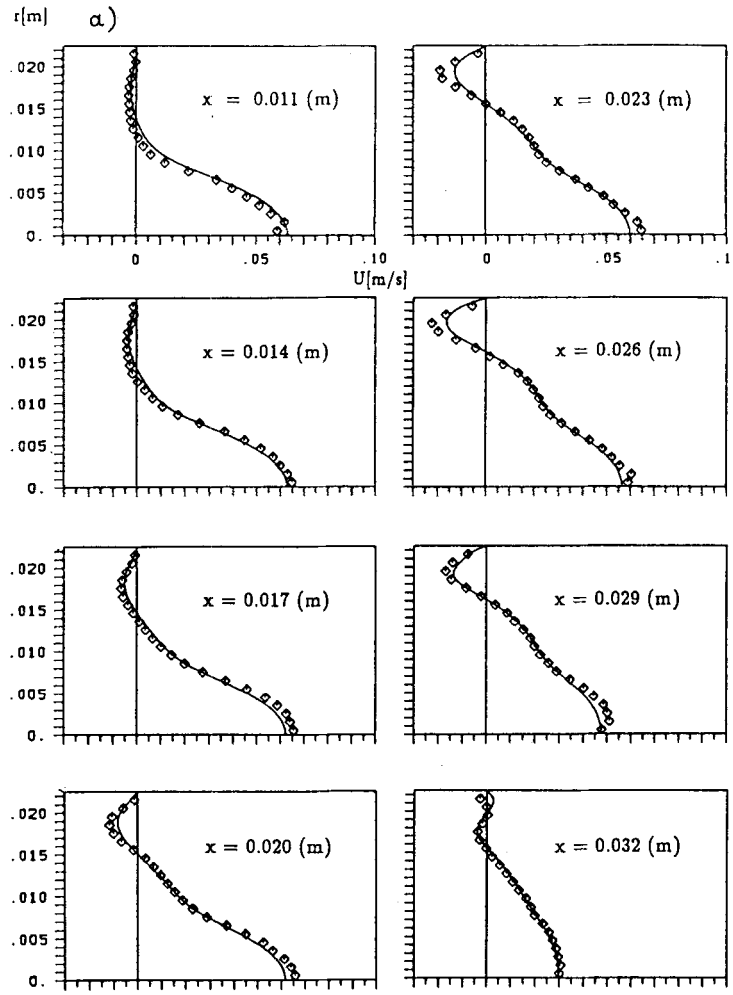

Figure 8. Comparison of computed and measured profiles of (a) axial and (b) radial velocity components for intake stroke of first cycle and piston position $x_p = 34{\cdot}847$ mm ($s_p^+ = 0{\cdot}69$)

line has just died out, as the zero axial velocities at $x = 0{\cdot}017$ and $0{\cdot}02$ m indicate. There are no vortices in the cylinder; however, the velocity profiles undergo rapid changes, from an almost uniform profile near the piston head ($x = 0{\cdot}026$ m), through strong peaks near the cylinder wall ($x = 0{\cdot}014$–$0{\cdot}02$ m) to strong peaks at the symmetry line close to the step plane. The agreement of predicted and measured velocities is again both qualitatively and quantitatively good. Discrepancies are only present for the radial velocity component close to the piston head. These discrepancies are no larger than the scatter of experimental data at some locations, although the discretization error might account for a few per cent disagreement at isolated peak locations.

CONCLUSIONS

The results of the analysis presented in the previous sections permit the following conclusions.

1. The axisymmetric piston-driven unsteady flow in a pipe with sudden expansion can be accurately

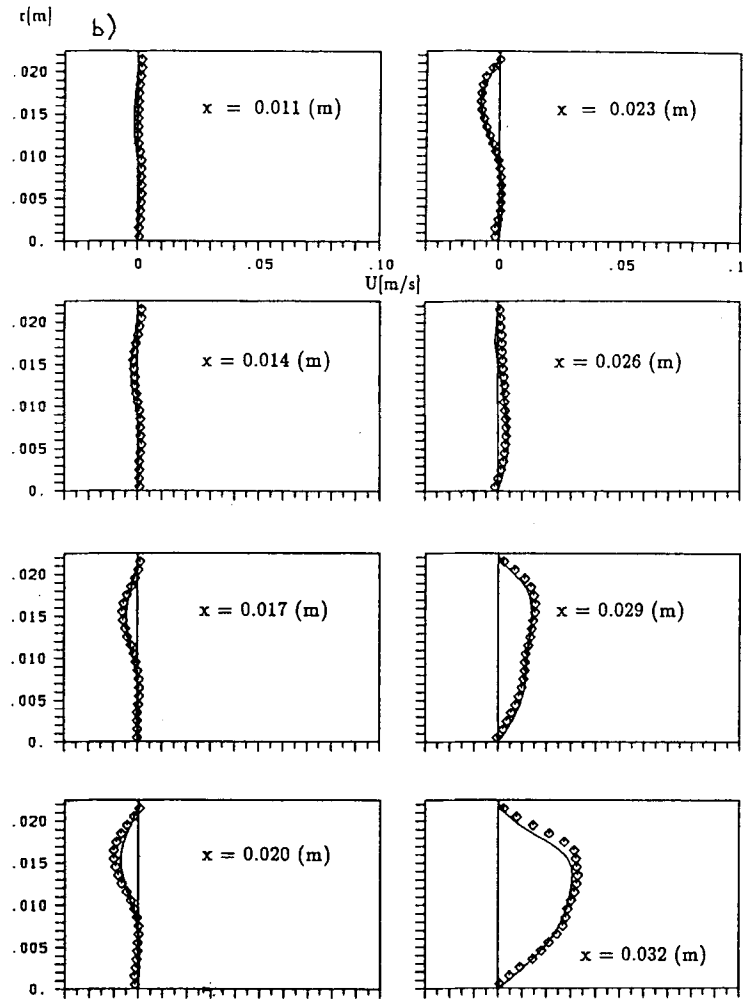

Figure 8b.

predicted by using a conservative finite volume method with moving grids. It has been shown that the discretization errors in space are more critical than the temporal discretization errors and that even with second-order spatial discetization, very fine grids are necessary in order to reduce the discretization error below 1% of the characteristic mean velocity. Calculations performed with a grid consisting of 256 × 80 CVs were found to be accurate enough to allow for an analysis of the flow features and comparison with experimental data, which showed good agreement.

2. In order to be able to estimate the discretization errors, calculations should be performed on a sequence of systematically refined grids. The errors are then proportional to the difference in solutions on two consecutive grids. It is also necessary to distinguish between the temporal and spatial discretization errors; this can be done by performing grid or step size dependence analysis while keeping the time step or spatial grid constant respectively. Spatial discretization errors in the present solution were in the largest part of the solution domain lower than 1%. Temporal discretization errors were found to be one order of magnitude lower than the spatial errors.

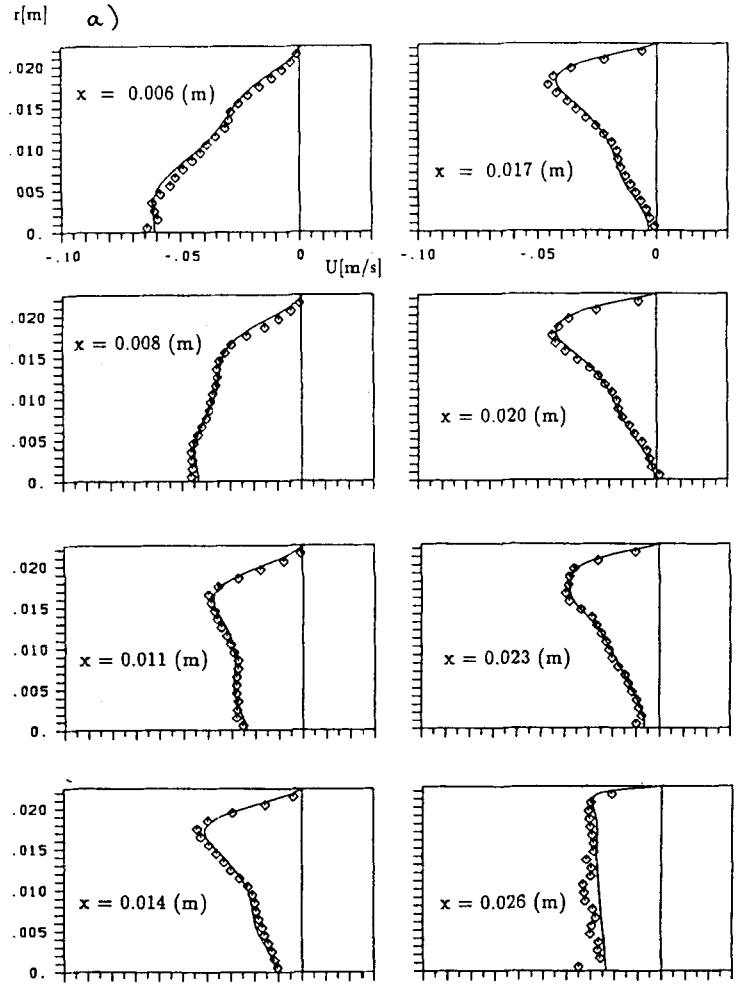

Figure 9. Comparison of computed and measured profiles of (a) axial and (b) radial velocity components for exhaust stroke of first cycle and piston position $x_p = 26{\cdot}876$ mm ($s_p^+ = 0{\cdot}29$)

3. When the spatial variations of the dependent variables require fine numerical grids but the temporal variation allows for larger time steps, fully implicit schemes for time discretization become attractive. However, these methods are only efficient when the multigrid algorithm is used to reduce the number of outer iterations per time step. In this study 10–15 outer iterations on the finest grid were performed with the multigrid algorithms, whereas the classical single-grid algorithm needed over an order of magnitude more iterations.
4. Analysis of axisymmetric piston-driven flow prediction shows good insight to the mean features of this class of flows and also indicates possible reasons for flow instabilities and cycle-to-cycle variations which occur at higher intake velocities. The velocity profiles with inflection points are prone to instabilities; another reason lies in the critical flow pattern near BDC and TDC, when some eddies disappear and new ones are formed.

A more detailed study of the instability of piston-driven flows is under way using the same solution algorithm but a three-dimensional anlaysis. It is expected that the experimentally observed[11] cycle-to-

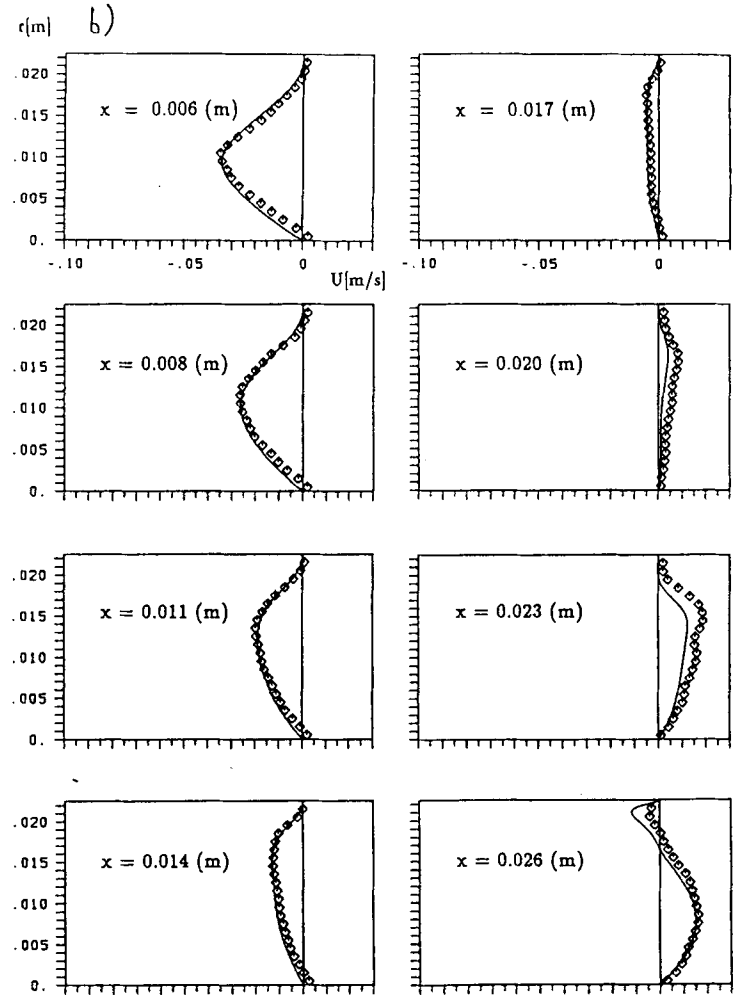

Figure 9b.

cycle variations can be reproduced and that a detailed analysis of the flow at critical stages will provide further clarification of the phenomena leading to flow instabilities.

REFERENCES

1. A. Brandt and N. Dinar, 'Multigrid solution to elliptic flow problems', in S. V. Parker (ed.), *Numerical Methods for Partial Differential Equations*, Academic, New York, 1979.
2. S. P. Vanka, 'A calculation procedure for three-dimensional steady recirculating flows using multigrid methods', *Comput. Methods Appl. Mech. Eng.*, **55**, 321–338 (1986).
3. G. Wittum, 'Distributive Iterationen für indefinite Systeme als Glätter im Mehrgitterverfahren am Beispiel der Strokes- und Navier–Stokes Gleichungen mit Schwerpunkt auf unvollständigen Zerlegungen', *Dissertation*, Universität Kiel, 1986.
4. M. Barcus, M. Perić and G. Scheuerer, 'A control volume based full multigrid procedure for the prediction of two-dimensional, laminar, incompressible flows', *Notes on Numerical Fluid Mechanics*, **20**, 9–16 (1988).
5. M. Hortmann, M. Periċc and G. Scheuerer, 'Finite volume multigrid prediction of laminar natural convection: bench-mark solutions', Int. j. numer. methods fluids, **11**, 189–207 (1990).
6. H. Ströll, F. Durst, M. Perić, J. C. F. Pereira and G. Scheuerer, 'Study of laminar, unsteady piston-cylinder flows', *ASME J. Fluids Eng.*, **115**, 687–693 (1993).

7. I. Demirdžić and M. Perić, 'Finite volume method for prediction of fluid flow in arbitrarily shaped domains with moving boundaries', *Int. j. numer. methods fluids*, **10**, 771–790 (1990).
8. S. V. Patankar and D. B. Spalding, 'A calculation procedure for heat, mass and momentum transfer in three-dimensional parabolic flows', *Int. J. Heat Mass Transfer*, **15**, 1787–1806 (1972).
9. H. L. Stone, 'Iterative solution of implicit approximation of multidimensional partial differential equations', *SIAM J. Numer. Anal.*, **5**, 530–558 (1968).
10. P. K. Khosla and S. G. Rubin, 'A diagonally dominant second-order accurate implicit scheme', *Comput. Fluids*, **2**, 207–209 (1974).
11. cH. Ströll, 'Entwicklung eines effizienten Verfahrens zur Berechnung instationärer laminarer Kolben–Zylinder-Strömungen', *Dissertation*, Universität Erlangen-Nürnberg, 1989.
12. F. Durst, T. Maxworthy and J. C. F. Pereira, 'Piston-driven, unsteady separation at a sudden expansion in a tube: flow visualization and LDA measurements', *Phys. Fluids A*, **1**, 1249–1260 (1989).